An efficient 3D non-hydrostatic model for predicting nonlinear wave interactions with fixed floating structures

Congfang Ai[a], Yuxiang Ma[a,*], Changfu Yuan[a], Zhihua Xie[b], Guohai Dong[a], Thorsten Stoesser[c]

[a]*State Key Laboratory of Coastal and Offshore Engineering, Dalian University of Technology, Dalian, China*

[b]*Hydro-environmental Research Centre, School of Engineering, Cardiff University, Cardiff, United Kingdom*

[c]*Department of Civil, Environmental and Geomatic Engineering, University College London, London, United Kingdom*

ABSTRACT

This paper presents a three-dimensional (3D) non-hydrostatic model for the prediction of the interaction between nonlinear waves and fixed floating structures. The model solves the incompressible Euler equation by use of a semi-implicit, fractional step algorithm. The water surface elevation is treated as a single-valued function of horizontal position. In order to deal with floating structures, a new numerical algorithm is proposed which combines the immersed boundary method and the global continuity equation in the pressurized region (flow region under the structure). This new algorithm holds the symmetry of the Poisson equation and therefore results in an efficient model. The developed model is validated with the data of two test cases involving 3D nonlinear wave interactions with a floating structure. The model results are compared with experimental data or results of other models. The proposed model exhibits generally good agreement with experimental data and/or other model results, demonstrating its accuracy in resolving 3D nonlinear wave interaction with floating structures.

Keywords: Non-hydrostatic model; Immersed boundary method; Wave-structure interactions; Floating structures

1. Introduction

Floating structures are very common in coastal and ocean engineering, because they can be constructed to create breakwaters, artificial islands, oil and natural gas storage facilities, etc. Accurate and efficient prediction of nonlinear waves interacting with floating structures has long been a concerned problem and is critical for the safety assessment and cost-effective design of floating structures. With the increase in computational power, numerical models based on the Navier-Stokes equations (NSE) to accurately predict nonlinear wave interactions with floating structures have received more attention from researchers recently.

One of the main challenges in applying NSE-based numerical models to wave-structure interactions is to improve the model efficiency. Many NSE-based numerical models employ the volume of fluid method (VOF) (Hu et al., 2016; Mohseni et al., 2018; Xie et al., 2017; Xie and Stoesser, 2020; Xie et al., 2020; Zhan et al., 2017) or the level-set method (Bihs et al., 2017; Vukčević et al., 2016) to capture the moving water-air interface. With these two methods, the models can accurately predict two-phase free surface flows with overturning free surfaces by refining the numerical grid. However, high computational cost of such NSE-based models limit their practical application. In order to reduce the high computational cost of NSE-based numerical models, one can discard the air phase and use the so-called free surface equation to capture the free surface. The free surface equation is derived by integrating the continuity equation over the water depth and meanwhile considering the kinematic free surface and bottom boundary conditions. As a result, the water surface elevation is treated as a single-valued function of the horizontal position. Non-hydrostatic models are just such models incorporating the free surface equation to deal with the moving free surface.

The development of non-hydrostatic models has been more than two decades, since Casulli and Stelling (1998) and Stansby and Zhou (1998) who simulated free surface flows by including non-hydrostatic effects. Nowadays, in addition to non-hydrostatic models for surface wave motions (Ai and Jin, 2012; Ai et al., 2011; Ai et al., 2019a; Bihs et al., 2019; Ma et al., 2012; Zijlema et al., 2011), there are also many non-hydrostatic models that are presented to resolve wave-structure interactions (Ai et al., 2018; Ai et al., 2019b; Ma et al., 2016; Ma et al., 2019; Rijnsdorp and Zijlema, 2016; Rijnsdorp et al., 2018), internal waves (Ai and Ding, 2016; Lai et al., 2010) and even tsunami propagation (Oishi et al., 2013). Most of the non-hydrostatic models for wave-structure interactions (Ai et al., 2018; Ai et al., 2019; Ma et al., 2016; Ma et al., 2019) employ the direct-forcing immersed boundary (IB) method, in which structures are treated as virtual bodies and the no-slip boundary condition is imposed on the structure's surface. However, the implementation of the IB method requires the Neumann boundary condition for pressure (NBCP) at the structure surface which complicates the coefficients of the Poisson equation, generally the most demanding part in the solution procedure of non-hydrostatic models. As a result, model efficiency is reduced due to the implementation of the IB method. Besides, Rijnsdorp and Zijlema (2016) developed a non-hydrostatic model to predict wave interactions with fixed floating structures without the incorporation of the IB method. In their model, the interaction between waves and a floating structure is considered as a combination of free-surface flows and pressurized flows and two global continuity equations are introduced to treat them, respectively.

In this paper, an efficient non-hydrostatic model for three-dimensional (3D) nonlinear wave interaction with a fixed floating structure is presented. The IB method is employed to deal with any shaped structures. However, to hold the symmetry of the Poisson equation and improve the model efficiency, the NBCP at the structure surface is replaced by the implementation of the global continuity equation in the pressurized region (Casulli and Stelling, 2013; Rijnsdorp and Zijlema, 2016). The developed model uses a semi-implicit algorithm to solve the Euler equations based on a grid system, which is built from a horizontal rectangular grid by adding dozens of layers in the vertical direction. Two selected examples are presented to validate the capability of the developed model in predicting nonlinear wave interactions with a fixed floating structure. Comparisons among the present model results, results obtained by OpenFOAM and experimental data are presented. OpenFOAM is an open-source computational fluid dynamics (CFD) software and employs the VOF method to capture the free surface. The model efficiency is also evaluated by the comparison between the developed model and other models. Notably, the model is extended from two former models (Ai et al., 2018; Ai et al., 2019a). One is a two-dimensional (2D) non-hydrostatic model (Ai et al., 2018), which predicts wave interactions with a fixed floating/suspended structure by using the IB method. However, the NBCP is imposed at the structure surface. The other is a 3D non-hydrostatic model just for surface wave motions (Ai et al., 2019a), which employs the explicit projection method to solve the Euler equations based on two semi-implicit algorithms. To the best of our knowledge, no 3D non-hydrostatic numerical models incorporating the IB method together with the global continuity equation in the pressurized region have been published to date.

2. Governing equations

The governing equations are the incompressible Euler equations, which can be expressed in the following forms by splitting the pressure into hydrostatic and non-hydrostatic components such that $p = g(\eta - z) + q$

$$\frac{\partial u}{\partial x} + \frac{\partial v}{\partial y} + \frac{\partial w}{\partial z} = 0 \tag{1}$$

$$\frac{\partial u}{\partial t} + \frac{\partial u^2}{\partial x} + \frac{\partial uv}{\partial y} + \frac{\partial uw}{\partial z} = -g\frac{\partial \eta}{\partial x} - \frac{\partial q}{\partial x} \tag{2}$$

$$\frac{\partial v}{\partial t} + \frac{\partial uv}{\partial x} + \frac{\partial v^2}{\partial y} + \frac{\partial vw}{\partial z} = -g\frac{\partial \eta}{\partial y} - \frac{\partial q}{\partial y} \tag{3}$$

$$\frac{\partial w}{\partial t} + \frac{\partial uw}{\partial x} + \frac{\partial vw}{\partial y} + \frac{\partial w^2}{\partial z} = -\frac{\partial q}{\partial z} \tag{4}$$

where u, v and w are the velocity components in the horizontal x and y and vertical z directions, respectively, t is the time, p is the normalized pressure divided by a constant reference density, q is the non-hydrostatic pressure component, and g is the gravitational acceleration. Notably, η is the free surface elevation in the free surface region and represents the piezometric head in the pressurized region (see Fig. 1).

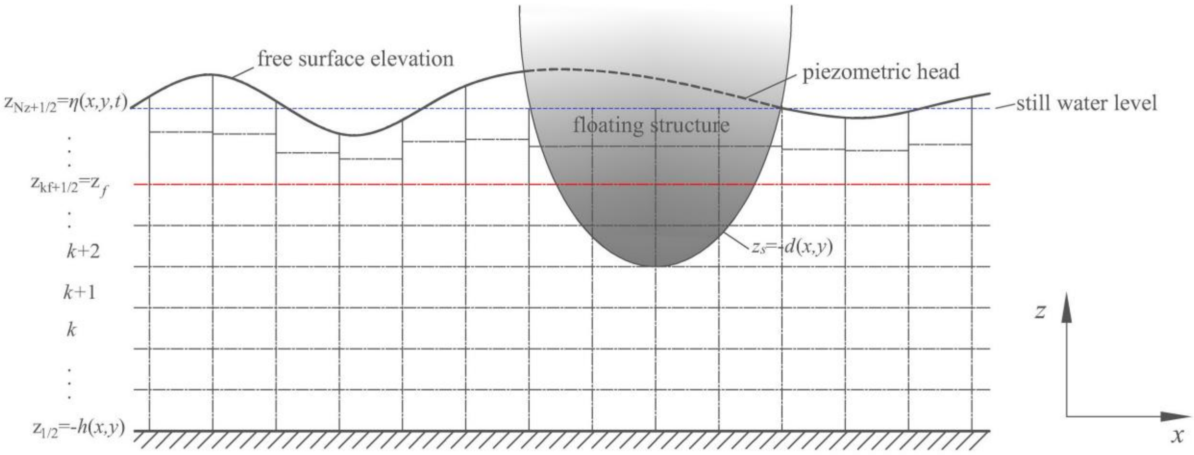

Fig. 1 Schematic diagram showing wave interaction with a fixed floating structure

Boundary conditions are required at all the boundaries of a 3D domain. In the free surface region, the following kinematic boundary is specified at the moving free surface $\eta(x, y, t)$

$$\frac{\partial \eta}{\partial t}+u\frac{\partial \eta}{\partial x}+v\frac{\partial \eta}{\partial y}=w|_{z=\eta} \tag{5}$$

In the pressurized region, the kinematic boundary at the body surface is

$$-u\frac{\partial d}{\partial x}-v\frac{\partial d}{\partial y}=w|_{z=-d} \tag{6}$$

where $z=-d(x,y)$ is the body surface (see Fig. 1).

At the impermeable bottom surface $z=-h(x,y)$, the kinematic boundary is

$$-u\frac{\partial h}{\partial x}-v\frac{\partial h}{\partial y}=w|_{z=-h} \tag{7}$$

By integrating the continuity Eq. (1) from $z=-h(x,y)$ to $z=\eta(x,y,t)$ and applying Leibniz' rule together with Eqs. (5) and (7), the following free surface equation is obtained:

$$\frac{\partial \eta}{\partial t}+\frac{\partial}{\partial x}\int_{z=-h}^{z=\eta}udz+\frac{\partial}{\partial y}\int_{z=-h}^{z=\eta}vdz=0 \tag{8}$$

Similarly, by means of integration of the continuity Eq. (1) from $z=-h(x,y)$ to $z=-d(x,y)$ and considering Eqs. (6) and (7), the following global continuity equation in the pressurized region is obtained:

$$\frac{\partial}{\partial x}\int_{z=-h}^{z=-d}udz+\frac{\partial}{\partial y}\int_{z=-h}^{z=-d}vdz=0 \tag{9}$$

Considering that the IB method is incorporated in the model and all the velocities inside the floating structure are zero, Eq. (9) can be rewritten as

$$\frac{\partial}{\partial x}\int_{z=-h}^{z=-\eta}udz+\frac{\partial}{\partial y}\int_{z=-h}^{z=-\eta}vdz=0 \tag{10}$$

Notably, Eq. (10) is only valid in the pressurized region and can be used to determine the piezometric head.

In addition, the impermeability condition is specified at all solid walls. At the inflow boundary, the normal velocity component is specified. At the outflow boundary, a sponge layer technique is implemented to minimize wave reflections.

3. Numerical algorithms

3.1 Integration of governing equations

Before using a semi-implicit, fractional step algorithm to solve the governing equations, they are first integrated in the vertical direction based on a general vertical boundary-fitted coordinate system (Ai et al., 2014). In such a vertical grid system (see Fig. 1), the horizontal levels are defined following Eq. (11).

$$z_{k+1/2}=\begin{cases} z_f+(k-k_f)[\eta(x,y,t)-z_f]/(N_z-k_f) & k>k_f \\ z_f & k=k_f \\ -h(x,y)+k[z_f+h(x,y)]/k_f & k<k_f \end{cases} \tag{11}$$

where k is the grid index in the z direction; N_z is the total number of vertical layers; $z_{k+1/2}=z_f$ is a predefined fixed level at the layer k_f (see Fig. 1). The horizontal levels above the z_f move with the free surface at each time, while below it they are fixed because of the immovable bottom surface in this study. The advantage of the general vertical boundary-fitted coordinate system in predicting steep water waves has been demonstrated in Ai et al. (2014).

By integrating the governing Eqs. (1)-(4) over the vertical layer k bounded by the levels $z_{k-1/2}$ and $z_{k+1/2}$, the following equations can be obtained:

$$\frac{\partial \Delta z_k}{\partial t}+\frac{\partial(\Delta zu)_k}{\partial x}+\frac{\partial(\Delta zv)_k}{\partial y}+\omega_{k+1/2}-\omega_{k-1/2}=0 \tag{12}$$

$$\begin{aligned}&\frac{\partial(\Delta zu)_k}{\partial t}+\frac{\partial(\Delta zuu)_k}{\partial x}+\frac{\partial(\Delta zuv)_k}{\partial y}+\omega_{k+1/2}u_{k+1/2}-\omega_{k-1/2}u_{k-1/2}\\ &+g\Delta z_k\frac{\partial \eta}{\partial x}+\Delta z_k\frac{\partial q}{\partial x}=0\end{aligned} \tag{13}$$

$$\begin{aligned}&\frac{\partial(\Delta zv)_k}{\partial t}+\frac{\partial(\Delta zuv)_k}{\partial x}+\frac{\partial(\Delta zvv)_k}{\partial y}+\omega_{k+1/2}v_{k+1/2}-\omega_{k-1/2}v_{k-1/2}\\ &+g\Delta z_k\frac{\partial \eta}{\partial y}+\Delta z_k\frac{\partial q}{\partial y}=0\end{aligned} \tag{14}$$

$$\begin{aligned}&\frac{\partial(\Delta zw)_k}{\partial t}+\frac{\partial(\Delta zuw)_k}{\partial x}+\frac{\partial(\Delta zvw)_k}{\partial y}+\omega_{k+1/2}w_{k+1/2}-\omega_{k-1/2}w_{k-1/2}\\ &+\Delta z_k\frac{\partial q}{\partial z}=0\end{aligned} \tag{15}$$

where $\Delta z_k = z_{k+1/2} - z_{k-1/2}$, and $\omega_{k+1/2}$ is the vertical velocity relative to layer level $z_{k+1/2}$.

After some manipulation (Ai et al., 2019a), Eqs. (13)-(15) can be written as follows:

$$\frac{\partial u_k}{\partial t} + Adv(u_k) = -g\frac{\partial \eta}{\partial x} - \frac{\partial q}{\partial x} \tag{16}$$

$$\frac{\partial v_k}{\partial t} + Adv(v_k) = -g\frac{\partial \eta}{\partial y} - \frac{\partial q}{\partial y} \tag{17}$$

$$\frac{\partial w_k}{\partial t} + Adv(w_k) = -\frac{\partial q}{\partial z} \tag{18}$$

where $Adv(u_k)$, $Adv(v_k)$ and $Adv(w_k)$ represent the advection terms for u_k, v_k and w_k, respectively.

Details of the integration procedures and the expressions for $Adv(u_k)$, $Adv(v_k)$ and $Adv(w_k)$ can be found in Ai et al. (2019a).

3.2 Semi-implicit algorithm

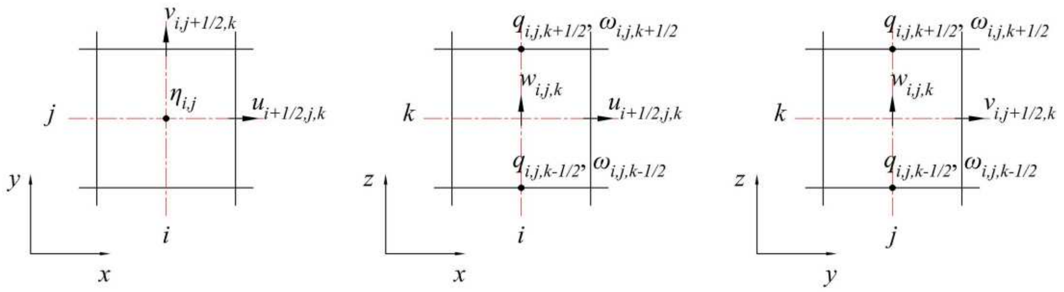

Fig. 2 Variables definition

The first step of an explicit projection method is to solve Eqs. (16)-(18) by neglecting the implicit contribution of the non-hydrostatic pressure. The resulting intermediate velocities $u^{n+1/2}_{i+1/2,j,k}$, $v^{n+1/2}_{i,j+1/2,k}$ and $w^{n+1/2}_{i,j,k}$ can be expressed as:

$$\frac{u^{n+1/2}_{i+1/2,j,k} - u^{n}_{i+1/2,j,k}}{\Delta t} + Adv\left(u^{n}_{i+1/2,j,k}\right) = -g\left(\frac{\partial \eta}{\partial x}\right)^{n+\theta}_{i+1/2,j} \tag{19}$$

$$\frac{v^{n+1/2}_{i,j+1/2,k} - v^{n}_{i,j+1/2,k}}{\Delta t} + Adv\left(v^{n}_{i,j+1/2,k}\right) = -g\left(\frac{\partial \eta}{\partial y}\right)^{n+\theta}_{i,j+1/2} \tag{20}$$

$$\frac{w_{i,j,k}^{n+1/2} - w_{i,j,k}^{n}}{\Delta t} + Adv\left(w_{i,j,k}^{n}\right) = 0 \tag{21}$$

where i and j are the grid indexes in the x and y directions, respectively. As shown in Fig. 2, the vertical velocity component w is directly defined at the cell center (i, j, k) and the horizontal velocity components u and v are positioned at cell faces $(i \pm 1/2, j, k)$ and $(i, j \pm 1/2, k)$, respectively. In addition, $\eta^{n+\theta} = (1-\theta)\eta^{n} + \theta\eta^{n+1}$, and θ is an implicitness factor.

In the second step, new velocities $u_{i+1/2,j,k}^{n+1}$, $v_{i,j+1/2,k}^{n+1}$ and $w_{i,j,k}^{n+1}$ are calculated by correcting the intermediate values after including the non-hydrostatic pressure.

$$\frac{u_{i+1/2,j,k}^{n+1} - u_{i+1/2,j,k}^{n+1/2}}{\Delta t} = -\left(\frac{\partial q}{\partial x}\right)_{i+1/2,j,k}^{n+1} + f_{IBF}(u_{i+1/2,j,k}) \tag{22}$$

$$\frac{v_{i,j+1/2,k}^{n+1} - v_{i,j+1/2,k}^{n+1/2}}{\Delta t} = -\left(\frac{\partial q}{\partial y}\right)_{i,j+1/2,k}^{n+1} + f_{IBF}(v_{i,j+1/2,k}) \tag{23}$$

$$\frac{w_{i,j,k}^{n+1} - w_{i,j,k}^{n+1/2}}{\Delta t} = -\left(\frac{\partial q}{\partial z}\right)_{i,j,k}^{n+1} + f_{IBF}(w_{i,j,k}) \tag{24}$$

where $f_{IBF}(u_{i+1/2,j,k})$, $f_{IBF}(v_{i,j+1/2,k})$ and $f_{IBF}(w_{i,j,k})$ are IB forces, which can be expressed as follows:

$$f_{IBF}(u_{i+1/2,j,k}) = \begin{cases} \dfrac{\hat{u}_{i+1/2,j,k}^{n+1} - u_{i+1/2,j,k}^{n+1/2}}{\Delta t} + \left(\dfrac{\partial q}{\partial x}\right)_{i+1/2,j,k}^{n+1} & \text{on or near the IB} \\ 0 & \text{elsewhere} \end{cases} \tag{25}$$

$$f_{IBF}(v_{i,j+1/2,k}) = \begin{cases} \dfrac{\hat{v}_{i,j+1/2,k}^{n+1} - v_{i,j+1/2,k}^{n+1/2}}{\Delta t} + \left(\dfrac{\partial q}{\partial y}\right)_{i,j+1/2,k}^{n+1} & \text{on or near the IB} \\ 0 & \text{elsewhere} \end{cases} \tag{26}$$

$$f_{IBF}(w_{i,j,k}) = \begin{cases} \dfrac{\hat{w}_{i,j,k}^{n+1} - w_{i,j,k}^{n+1/2}}{\Delta t} + \left(\dfrac{\partial q}{\partial z}\right)_{i,j,k}^{n+1} & \text{on or near the IB} \\ 0 & \text{elsewhere} \end{cases} \tag{27}$$

where the IB velocities $\hat{u}_{i+1/2,j,k}^{n+1}$, $\hat{v}_{i,j+1/2,k}^{n+1}$ and $\hat{w}_{i,j,k}^{n+1}$ are calculated following a linear interpolation method presented by Fadlun et al. (2000) to impose a no-slip boundary condition at the structure surface. For details about the implementation of the

IB method, the reader can refer to Ai et al. (2018).

The continuity Eq. (1) is discretized by the semi-implicit method together with the finite difference method.

$$\begin{cases} \dfrac{(u^{n+\theta}_{i+1/2,j,k}+u^{n+\theta}_{i+1/2,j,k-1})-(u^{n+\theta}_{i-1/2,j,k}+u^{n+\theta}_{i-1/2,j,k-1})}{2\Delta x} \\ +\dfrac{(v^{n+\theta}_{i,j+1/2,k}+v^{n+\theta}_{i,j+1/2,k-1})-(v^{n+\theta}_{i,j-1/2,k}+v^{n+\theta}_{i,j-1/2,k-1})}{2\Delta y} \\ +\dfrac{w^{n+\theta}_{i,j,k}-w^{n+\theta}_{i,j,k-1}}{\Delta z_{i,j,k-1/2}}=0, \qquad \text{for } k=2,\ldots,N_z \\ \dfrac{u^{n+\theta}_{i+1/2,j,1}-u^{n+\theta}_{i-1/2,j,1}}{\Delta x}+\dfrac{v^{n+\theta}_{i,j+1/2,1}-v^{n+\theta}_{i,j-1/2,1}}{\Delta y}+\dfrac{w^{n+\theta}_{i,j,1}}{\Delta z_{i,j,1/2}}=0, \qquad \text{for } k=1 \end{cases} \tag{28}$$

where $\Delta z_{i,j,k-1/2}=(\Delta z_{i,j,k-1}+\Delta z_{i,j,k})/2$ and $\Delta z_{i,j,1/2}=\Delta z_{i,j,1}/2$. Notably, the continuity equation is discretized in a half bottom cell for $k=1$.

The semi-implicit finite difference approximation of the global continuity Eq. (8) is

$$\begin{aligned} &\frac{\eta^{n+1}_{i,j}-\eta^{n}_{i,j}}{\Delta t}+\frac{1}{\Delta x}\left(\sum_{k=1}^{N_z}\Delta z^{n}_{i+1/2,j,k}u^{n+\theta}_{i+1/2,j,k}-\sum_{k=1}^{N_z}\Delta z^{n}_{i-1/2,j,k}u^{n+\theta}_{i-1/2,j,k}\right) \\ &+\frac{1}{\Delta y}\left(\sum_{k=1}^{N_z}\Delta z^{n}_{i,j+1/2,k}v^{n+\theta}_{i,j+1/2,k}-\sum_{k=1}^{N_z}\Delta z^{n}_{i,j-1/2,k}v^{n+\theta}_{i,j-1/2,k}\right)=0 \end{aligned} \tag{29}$$

Similarly, Eq. (10) is discretized by the following fully implicit finite difference method for stability

$$\begin{aligned} &\frac{1}{\Delta x}\left(\sum_{k=1}^{N_z}\Delta z^{n}_{i+1/2,j,k}u^{n+1}_{i+1/2,j,k}-\sum_{k=1}^{N_z}\Delta z^{n}_{i-1/2,j,k}u^{n+1}_{i-1/2,j,k}\right) \\ &+\frac{1}{\Delta y}\left(\sum_{k=1}^{N_z}\Delta z^{n}_{i,j+1/2,k}v^{n+1}_{i,j+1/2,k}-\sum_{k=1}^{N_z}\Delta z^{n}_{i,j-1/2,k}v^{n+1}_{i,j-1/2,k}\right)=0 \end{aligned} \tag{30}$$

Eq. (12) is also discretized by the semi-implicit method and is used to compute $\omega^{n+1}_{i,j,k+1/2}$. This gives

$$\begin{aligned} &\frac{\Delta z^{n+1}_{i,j,k}-\Delta z^{n}_{i,j,k}}{\Delta t}+\frac{1}{\Delta x}(\Delta z^{n}_{i+1/2,j,k}u^{n+\theta}_{i+1/2,j,k}-\Delta z^{n}_{i-1/2,j,k}u^{n+\theta}_{i-1/2,j,k}) \\ &+\frac{1}{\Delta y}(\Delta z^{n}_{i,j+1/2,k}v^{n+\theta}_{i,j+1/2,k}-\Delta z^{n}_{i,j-1/2,k}v^{n+\theta}_{i,j-1/2,k})+\omega^{n+\theta}_{i,j,k+1/2}-\omega^{n+\theta}_{i,j,k-1/2}=0 \end{aligned} \tag{31}$$

The non-hydrostatic pressures in Eqs. (22)-(24) are determined by solving the Poisson equation, which is obtained by substituting Eqs. (22)-(24) into Eq. (28). The resulting Poisson equation can be written in the following matrix form:

$$\mathbf{A}\mathbf{q} = \mathbf{b} \tag{32}$$

where $\mathbf{A}$ is a sparse coefficient matrix, $\mathbf{q}$ is a vector of the non-hydrostatic pressure, and $\mathbf{b}$ is a known vector related to explicit and intermediate velocities.

There is no implementation of the NBCP at the structure surface in Eq. (32), because Eq. (10) is included in the model. As a result, the coefficients of the matrix $\mathbf{A}$ are quite similar to those presented in Ai et al. (2019a). Moreover, $\mathbf{A}$ is symmetric and contains 10 nonzero diagonals in bottom cells and 15 nonzero diagonals in other cells. Notably, the implementation of the global continuity equation results in the symmetric system of Eq. (32). The Poisson equation presented by Ai et al. (2018) is a non-symmetric system and is solved less efficiently than Eq. (32).

The computational procedure is summarized as follows:

(1) Substitute Eqs. (19), (20), (22) and (23) into Eqs. (29) and (30), respectively, yielding a diagonally dominant and symmetric system for η^{n+1}, which is solved by the conjugate gradient method by neglecting the implicit non-hydrostatic pressure.

(2) Compute the intermediate velocities $u^{n+1/2}$, $v^{n+1/2}$ and $w^{n+1/2}$ by using Eqs. (19)-(21) and implement the IB method to determine all the intermediate IB velocities nearby the structure surface but outside the structure.

(3) Solve Eq. (32) to obtain the non-hydrostatic pressure q^{n+1} by means of the conjugate gradient method.

(4) Repeat steps 1 to 3 until convergence is reached.

(5) Compute the new velocities u^{n+1}, v^{n+1} and w^{n+1} by using Eqs. (22)-(24) and implement the IB method to calculate the new IB velocities.

(6) Compute the vertical velocity relative to the layer level ω^{n+1} by using Eq. (31).

Notably, implicitness factors θ in all the equations are set to 0.5 and 1.0 for free surface and pressurized flows, respectively for stability.

4. Numerical results

4.1 Regular wave incident on a box-shaped ship fixed in a harbor

In the first test case, a regular wave incident on a box-shaped ship fixed in a harbor is considered. The numerical results are compared with experimental data from Wang et al. (2011). The computational domain is shown in Fig. 3, in which the floating box-shaped ship has the dimension of $L_x = 0.6$ m, $L_y = 2.0$ m and $L_z = 0.45$ m and is positioned at (21.8 m, 0.0 m, 0.285 m). The draft of the ship is 0.24 m. In the working area, the still water depth is $h = 0.3$ m. The incident regular wave train with a wave height $H_0 = 3.0$ cm and a wave period $T_0 = 3.0$ s is specified at the left boundary of the domain. Free surface elevations at 14 wave gauges were recorded in the experiment. The incident wave is generated following linear wave theory.

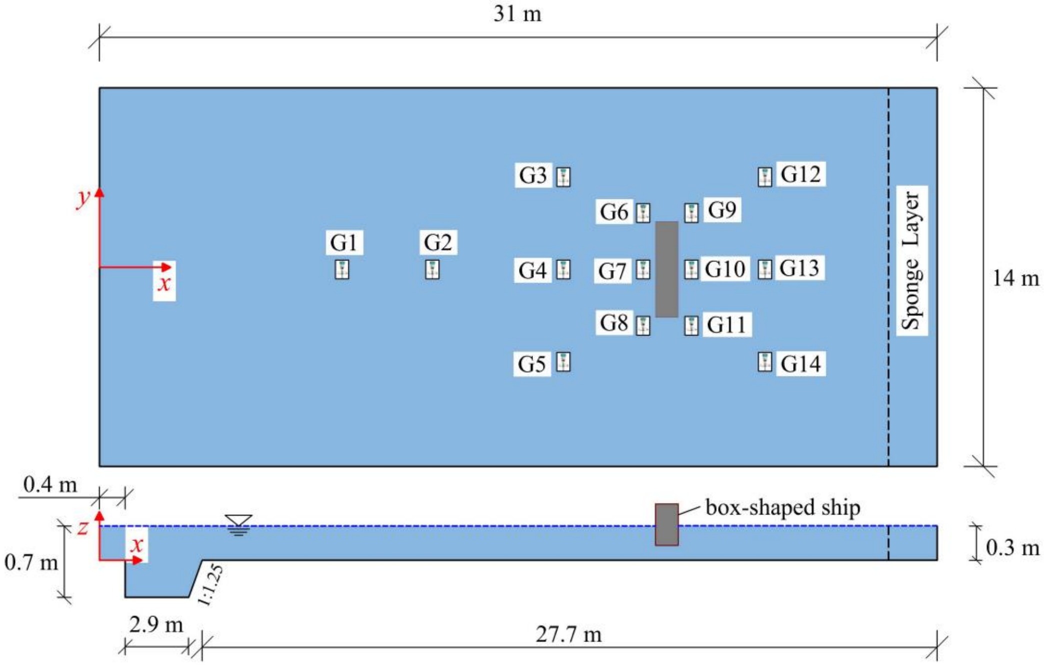

Fig. 3 Sketch of the model setup including the location of water surface elevation measurement stations

Table 1 Grid configurations used in the grid convergence study

Mesh	Mesh1	Mesh2	Mesh3	Mesh4
Horizontal grid size $\Delta x = \Delta y$ (m)	0.1	0.05	0.05	0.025
Total number of vertical layers N_z	5	5	10	5
z_f used in the vertical grid system (m)	-0.24	-0.24	-0.24	-0.24
k_f used in the vertical grid system	2	2	4	2

Total grid number	280,000	1,120,000	2,240,000	4,480,000

First of all, grid convergence tests are carried out using four different grid configurations (see Table 1). In all four simulations, uniform horizontal grids are employed. Table 1 provides detailed information about the four grid configurations. The calculated wave forces on the structure obtained by the four grid configurations are plotted in Fig. 4. The nondimensional wave forces $\overline{F}_x$ and $\overline{F}_z$ are defined by $\overline{F}_x = F_x/(\rho g H_0 L_x L_y)$ and $\overline{F}_z = F_z/(\rho g H_0 L_x L_y)$, respectively where F_x and F_z are the wave forces in the x and z directions, respectively. The simulation on Mesh1 predicts smaller values of positive wave forces than the simulations on the other grids. Numerical results obtained on Mesh2, Mesh3 and Mesh4 are quite close to each other. Considering the computational efficiency, results based on Mesh2 are presented in the following.

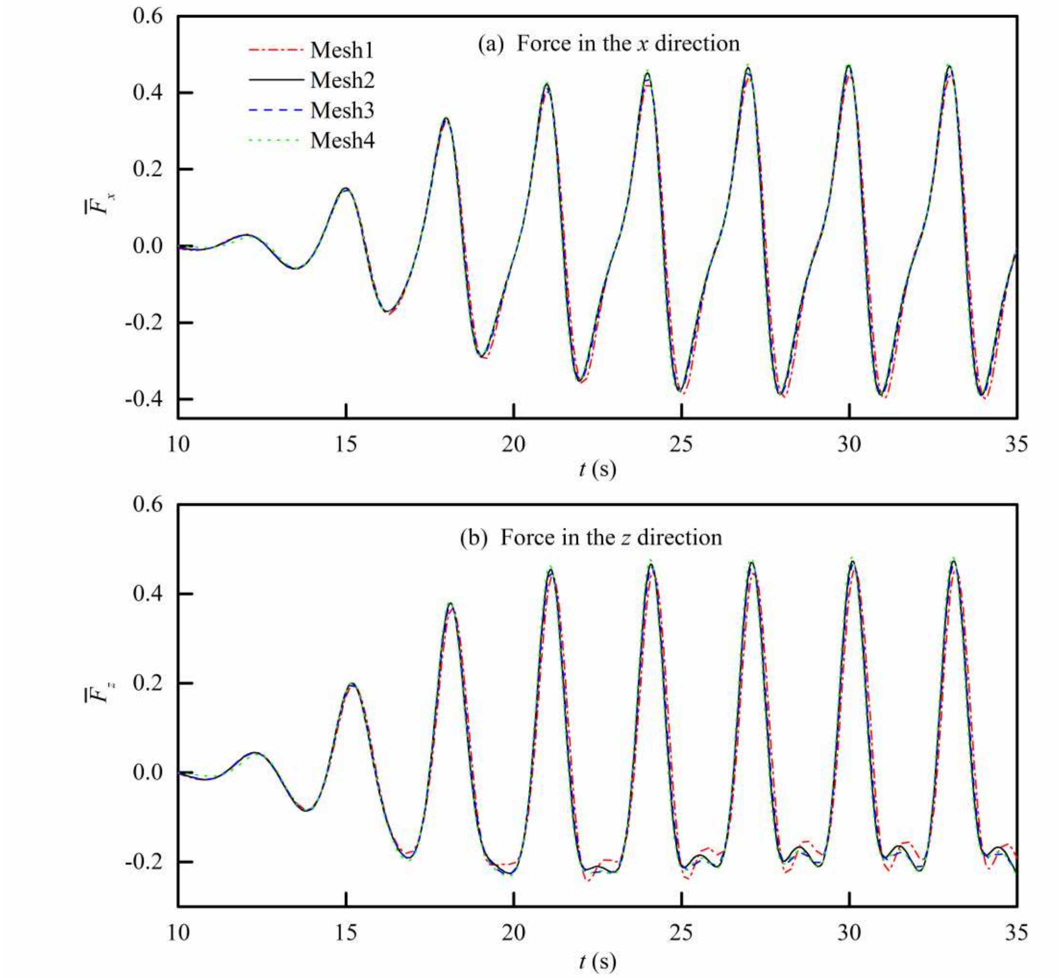

Fig. 4 Wave forces on the box-shaped ship as a function of time obtained on the four different

grid configurations (a) horizontal force and (b) vertical force

Fig. 5 shows water surface elevations as computed by the proposed non-hydrostatic model (dashed red line), an OpenFOAM solver (solid black line) and experimental data at ten wave gauges. OpenFOAM solves the Euler equations for two incompressible phases (water and air) using the VOF method to track the moving interface between the two phases. In the OpenFOAM simulation, the horizontal domain in the y direction is reduced to 8 m to improve the computational efficiency and in the z direction it is extended upwards by 0.3 m to include the air phase and horizontal and vertical grid sizes are set to $\Delta x = \Delta y = 0.05$ m and $\Delta z = 0.01$ m, respectively. Notably, to accurately capture the free surface a fine grid in the vertical direction is employed in the OpenFOAM simulation. The results of both models are close and are in generally good agreement with the experimental data. However, the developed model predicts larger wave heights than OpenFOAM at gauge points G6 and G7 in front of the structure and gauge points G9, G10, G12 and G13 behind it.

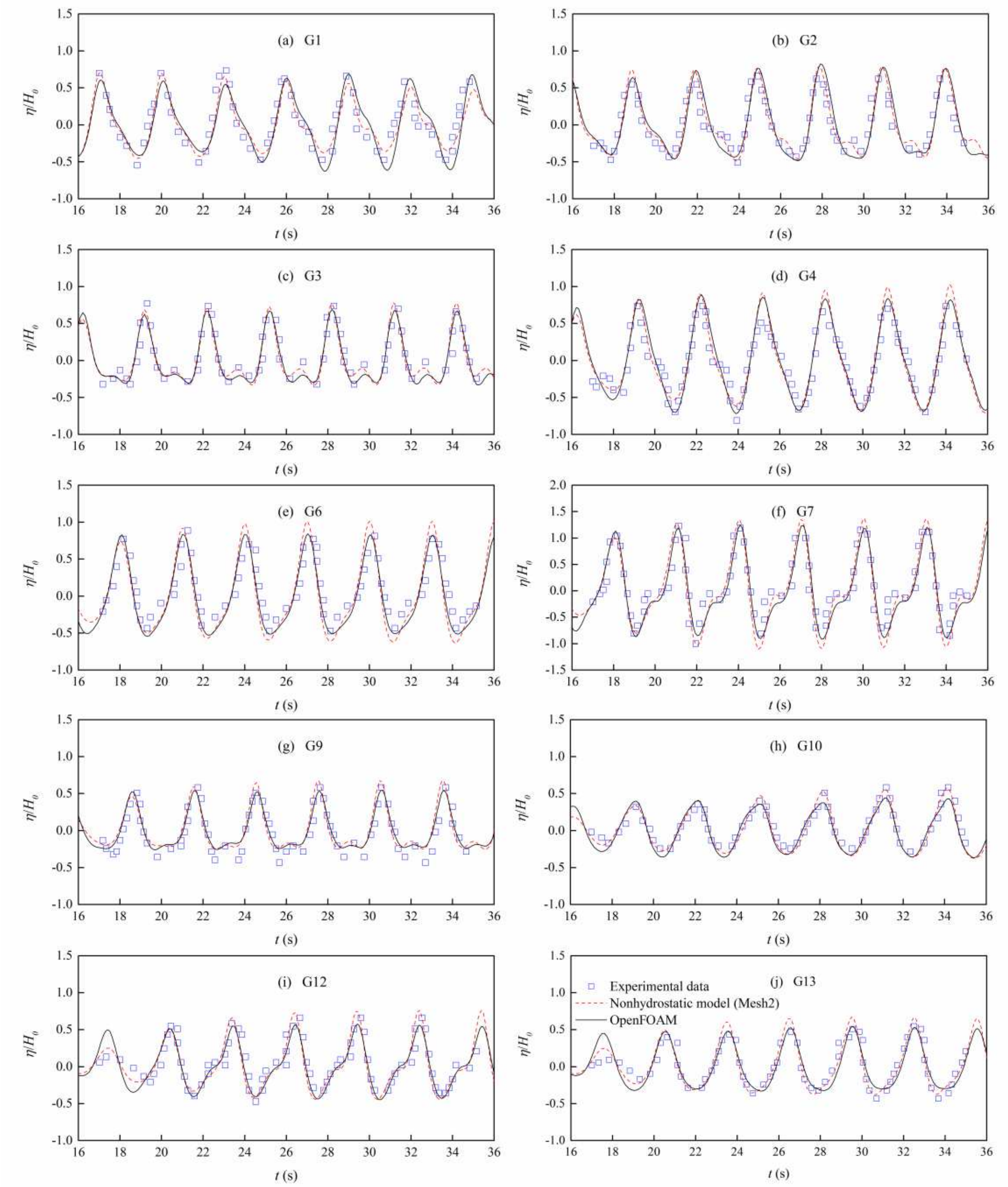

Fig. 5 Time histories of the water surface elevation as predicted by the proosed non-hydrostatic model, OpenFOAM together with experimental data at 10 wave gauges.

Fig. 6 presents time histories of the two nondimensional wave forces in the x and z directions as calculated by the non-hydrostatic model and OpenFOAM. The profiles of the two calculated wave forces are quite similar. However, the developed model predicts larger values of positive and negative wave forces than OpenFOAM. This is due to the aforementioned fact that larger wave heights around the structure are simulated by the developed model.

Table 2 provides the comparison of the computational efficiency between the two sets of non-hydrostatic models and OpenFOAM. The two sets of non-hydrostatic models include the non-hydrostatic model with the implementation of Eq. (10) and the non-hydrostatic model with the implementation of the NBCP. For all the simulations, the total simulation time is up to 45 s. However, the constant time step of $\Delta t = 0.025$ s is used for both the non-hydrostatic models, while for OpenFOAM the time step is controlled by setting the maximum CFL number to CFL=0.25. The two non-hydrostatic models were run on a Windows 7 desktop computer with an Intel(R) Core(TM) i7-7700K CPU, which is a quad-core processor and has a base frequency of 4.2 GHz with 8 MB L3 cache. OpenFOAM was implemented on a workstation equipped with Linux operating system, in which the CPU has 14 cores with a base frequency of 2.4 GHz and 35 MB L3 cache. The two non-hydrostatic models use the C# shared memory library for parallelization, while OpenFOAM is an openMP/MPI parallelized solver. The CPU times required by the non-hydrostatic model with the implementation of Eq. (10) and the non-hydrostatic model with the implementation of the NBCP are 1.59 h and 12.14 h, respectively. The computational time for OpenFOAM is 38.18 h. The non-hydrostatic model with the implementation of Eq. (10) is more efficient than the non-hydrostatic model with the implementation of the NBCP. OpenFOAM is more time consuming than the two non-hydrostatic models, mainly because a fine vertical grid is used in the OpenFOAM simulation.

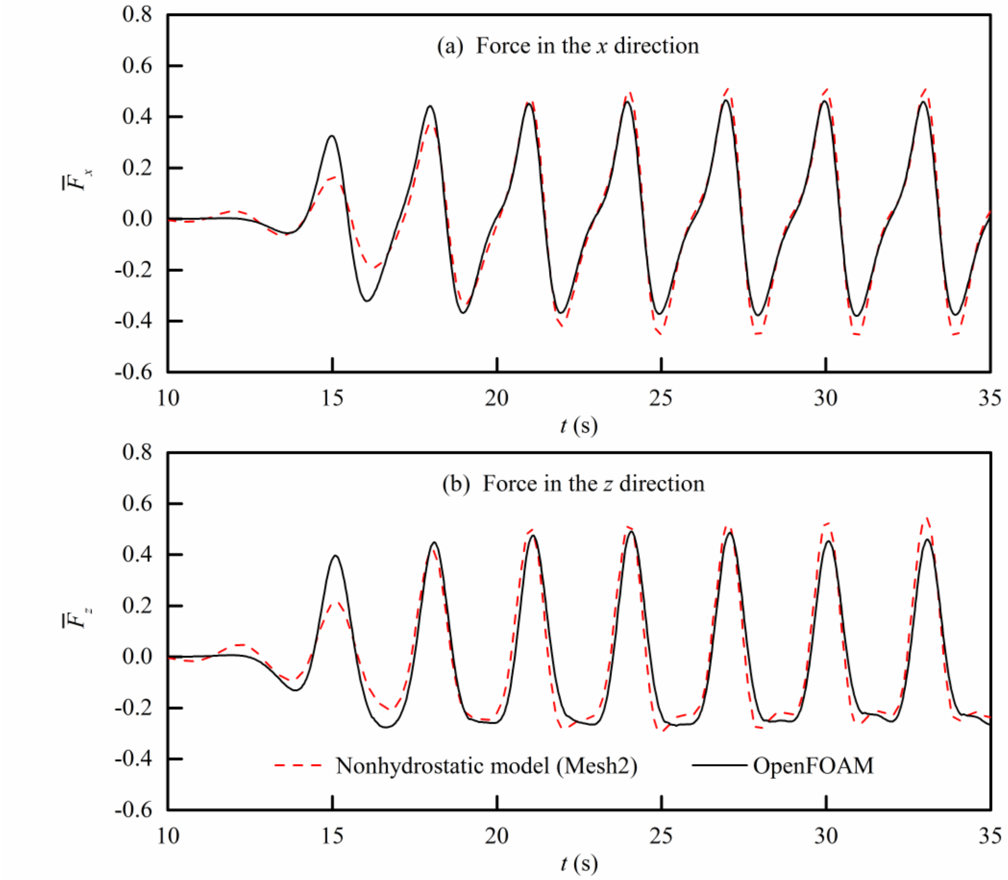

Fig. 6 Comparisons of wave forces in the x and z directions between the present model results and the OpenFOAM results.

Table 2 Computational efficiency for the two sets of non-hydrostatic models and OpenFOAM

	Computational environment	Total grid number	CPU time (h)
Non-hydrostatic model with Eq. (10)	Operating system: Windows 7 CPU: Intel(R) Core(TM) i7-7700K, 4 cores, 4.2 GHz L3: 8 MB	1,120,000	1.59
Non-hydrostatic model with the NBCP			12.14
OpenFOAM	Operating system: Linux CPU: Intel(R) Xeon(R) E5-2680 v4, 14 cores, 2.4 GHz L3: 35 MB	6,365,600	38.18

4.2 Focused wave interactions with a fixed FPSO

Table 3 Incident wave parameters

	Input wave amplitude A (m)	Working water depth h (m)	Wave steepness KA	Incident wave angle α (°)
Case 12BT1	0.09128	2.93	0.18	0
Case 22BT1	0.08930		0.17	10

Experiments on focused wave interactions with a fixed, scale-model, floating production storage and offloading (FPSO) vessel were presented by the CCP-WSI (Collaborative Computational Project in Wave Structure Interaction) Blind Test Series 1 (http://www.ccpwsi.ac.uk/blind_test_series_1). A total of six groups of focused waves with three different wave steepnesses and three different wave directions were considered in the experiments. In this study, Case 12BT1 and Case 22BT1 are reproduced numerically with the goal to validate the developed model for this type of wave-structure interaction. For the two test cases, the main wave parameters are listed in Table 3 and the computational domain is sketched in Fig. 7. As provided in Table 3, the input amplitudes of the two wave groups are slightly different. Case 12BT1 is a normal incident test case, whereas Case 22BT1 is corresponding to a 10° incident wave angle. The FPSO consists of two semicylinders and a cuboid. The height of the FPSO is 0.303 m and the draft is 0.153 m. The horizontal dimensions of the FPSO and the locations of the wave gauges are shown in Fig. 8. Fig. 9 details the positions of pressure sensors on the FPSO for the two test cases. The available experimental data include the runup at various positions around the FPSO, the free surface elevation in the vicinity of the FPSO and the pressure on the bow and can be downloaded from http://www.ccpwsi.ac.uk/blind_test_series_1.

To generate the two unidirectional focused wave groups, the following normal velocity components are imposed at the left inflow boundary:

$$u(x,z,t)=\sum_{n=1}^{N}\left\{a_n\omega_n\frac{\cosh\left[k_n(h+z)\right]}{\sinh(k_nh)}\cos\left[k_ny\sin(\alpha)-\omega_nt+\varphi_n\right]\right\} \tag{33}$$

where N is the number of frequency components; a_n defines the amplitude of each component; k_n and ω_n are the wavenumber and frequency of each component, respectively, satisfying the linear dispersion relationship; and φ_n denotes the phase angle of each component.

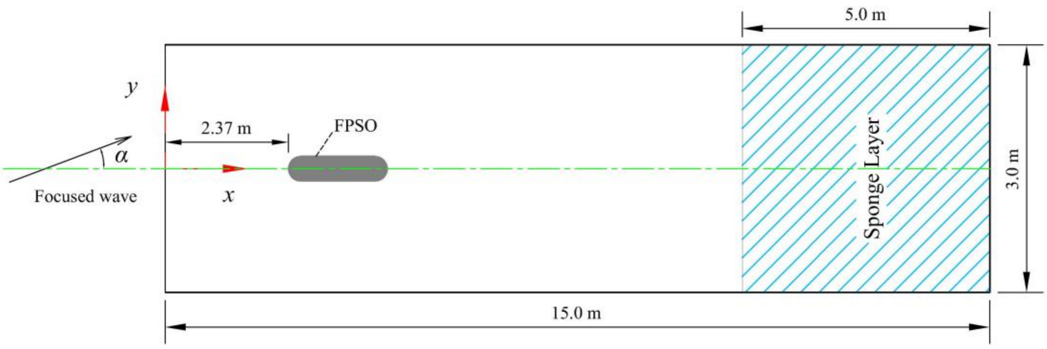

Fig. 7 Sketch of the model setup

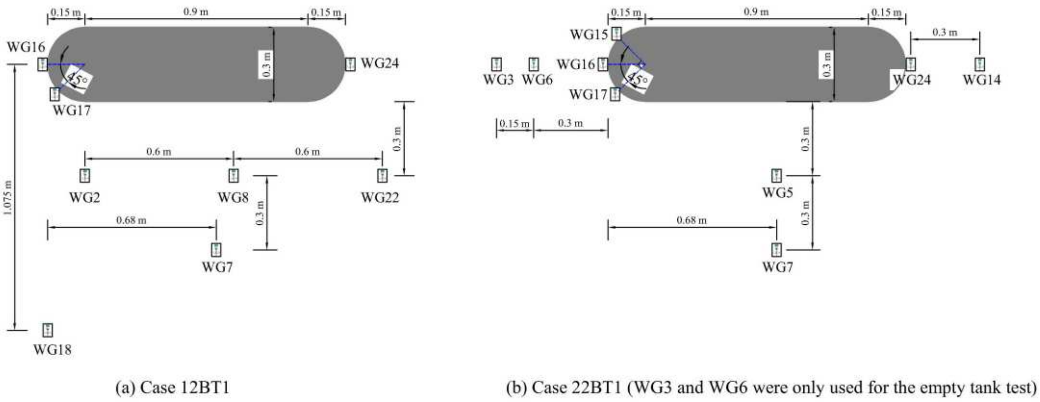

Fig. 8 Dimension of the FPSO and wave gauge layout

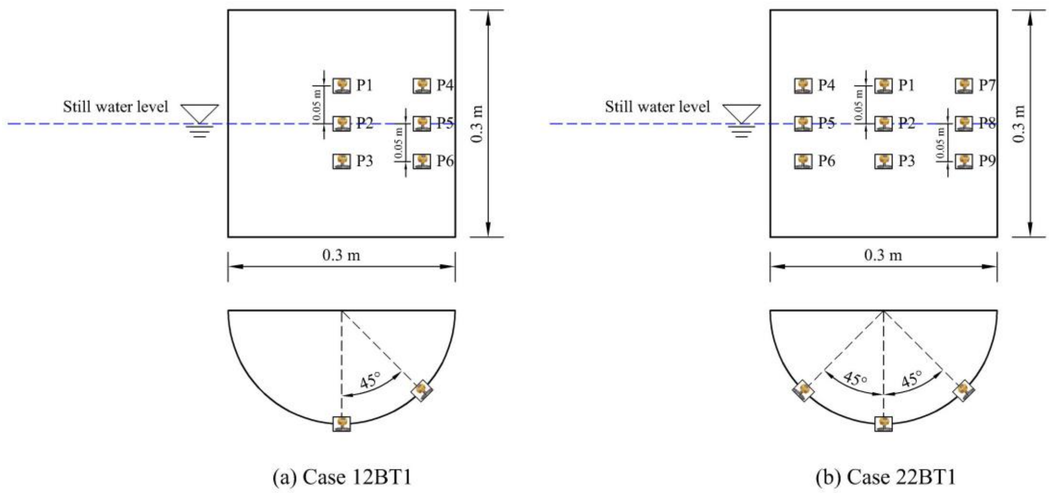

Fig. 9 Pressure sensor layout in front of the FPSO

To validate wave generations for Case 12BT1 and Case 22BT1, numerical simulations are firstly performed in the absence of the FPSO. A horizontal grid spacing of Δx = 0.025 m and time step of Δt = 0.005 s are used in both simulations. The vertical grid system is constructed by using 42 layers with z_f = -0.1465 m and k_f = 38. However, only one grid is employed in the y direction, because the generated waves are homogeneous (quasi-two-dimensional) in that direction. Time histories of calculated and experimentally-measured free surface elevations at two wave gauge locations for Case 12BT1 and Case 22BT1 without the FPSO are depicted in Figs. 10 and 11, respectively. The gauge WG16 corresponds to the bow of the FPSO and is the theoretical focus location for both cases. Generally, the present model results are in good agreement with the experimental data for both test cases.

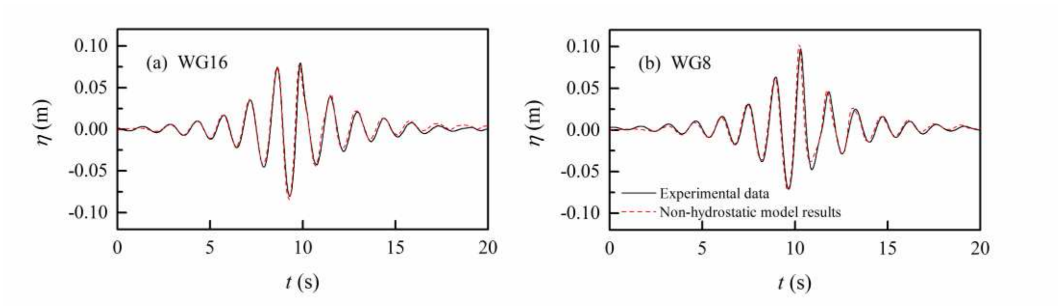

Fig. 10 Comparisons of the time histories of the free surface elevation between the present results and experimental data for Case 12BT1 without the FPSO.

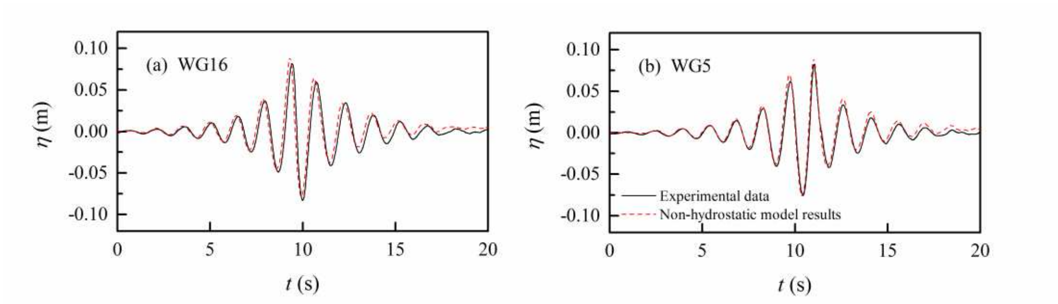

Fig. 11 Comparisons of the time histories of the free surface elevation between the present results and experimental data for Case 22BT1 without the FPSO.

In the numerical simulations with the FPSO present, grid convergence tests reveal that horizontal spacing of $\Delta x = \Delta y = 0.025$ m and a vertical grid system of 42 layers with $z_f = -0.1465$ m and $k_f = 38$ are adequate. The time step is set to $\Delta t = 0.005$ s and the total simulation time is up to 20 s. Figs. 12 and 13 show time histories of the water surface elevation as predicted by the present model and the measured experimental data for Case 12BT1 and Case 22BT1, respectively. The published results (Ransley et al., 2019) obtained by OpenFOAM with the waves2Foam solver are also plotted at gauge WG16 for comparison. In the waves2Foam solver, focused waves are also generated by the linear superposition of first-order wave components. However, OpenFOAM employs an unstructured grid with a typical grid size of 0.025 m in the region of the free surface and 0.002625 m around the FPSO to discretize the computational domain. For the Case 12BT1, the predictions of the present non-hydrostatic model generally agree well with the experimental data except for gauge

WG16, in which the wave profile is quite close to that obtained by OpenFOAM and both models overestimate the runup. For Case 22BT1, the non-hydrostatic model predictions are also quite similar to the OpenFOAM's results at gauge WG16 and are in good agreement with the experimental data at gauge WG7. However, the present model slightly overpredicts the runup around the FPSO.

Figs. 14 and 15 show the measured and calculated time histories of the pressure on the bow for Case 12BT1 and Case 22BT1, respectively. The aforementioned OpenFOAM results are plotted at gauge P2 for comparison. The non-hydrostatic model captures the overall profiles of the measurements, but appears to underestimate the pressure at gauges P4 and P5 for Case 12BT1 and overestimate it at most gauge locations with the exception of gauge P3 for Case 22BT1. The overall agreement between the present model and OpenFOAM is generally good. However, the present model slightly overpredicts the two peak values of pressure at gauge P2 for Case 22BT1.

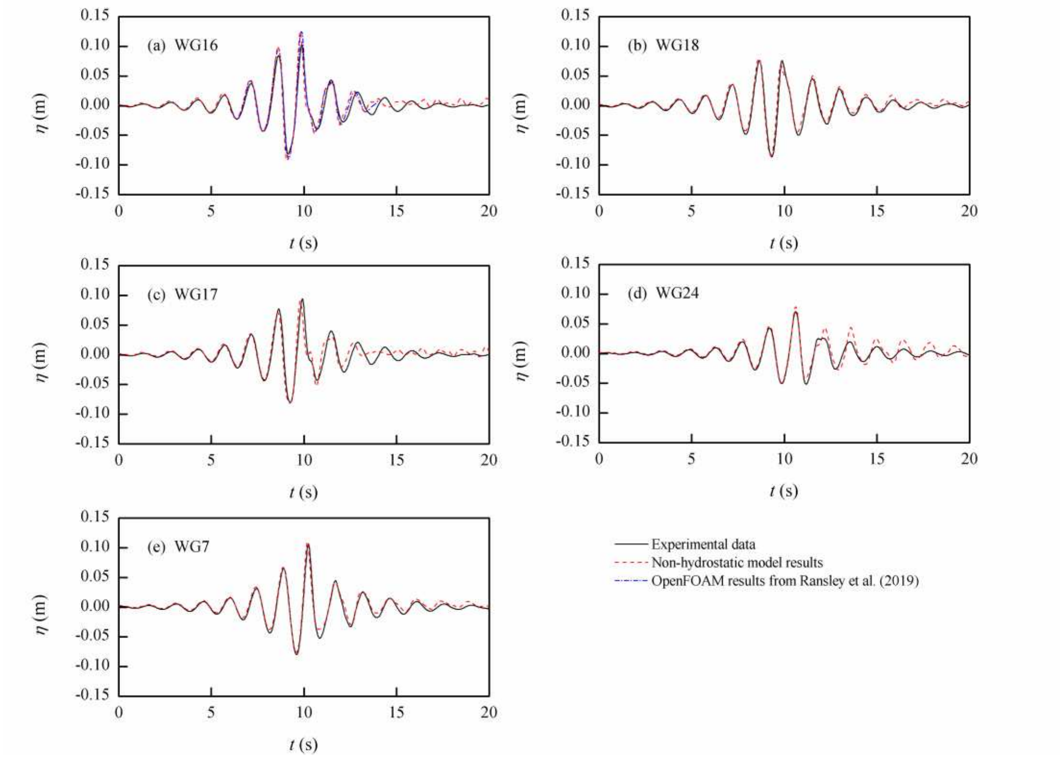

Fig. 12 Comparisons of the time histories of the free surface elevation between the present model results and experimental data for Case 12BT1.

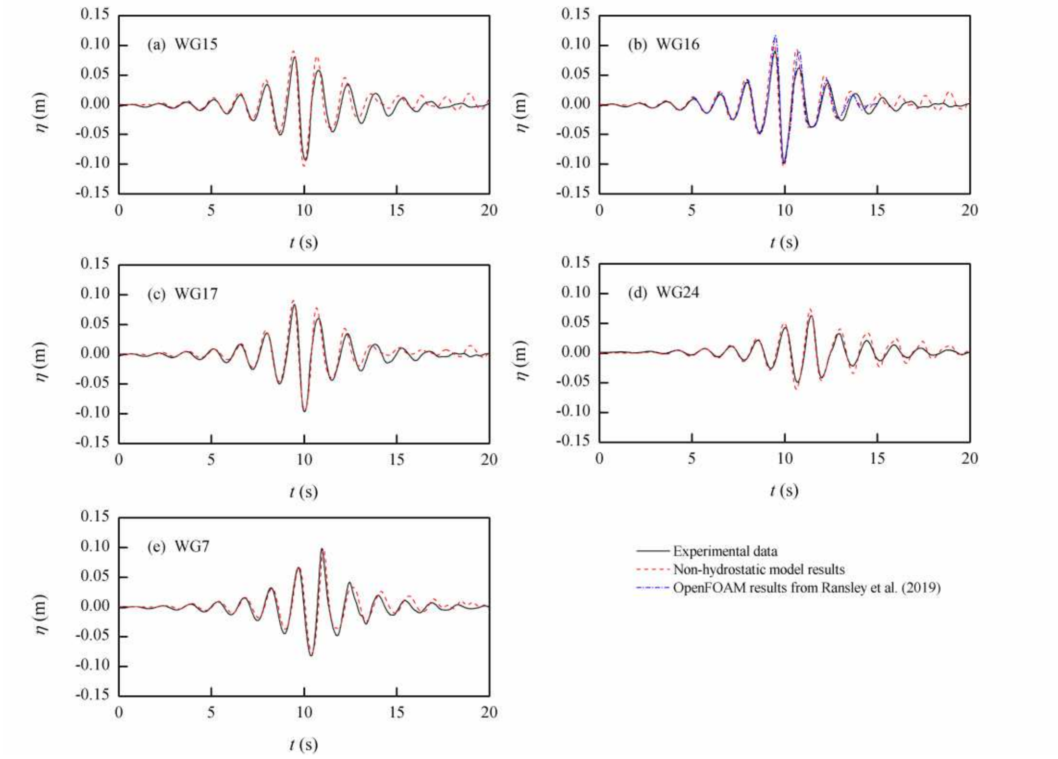

Fig. 13 Comparisons of the time histories of the free surface elevation between the present model results and experimental data for Case 22BT1.

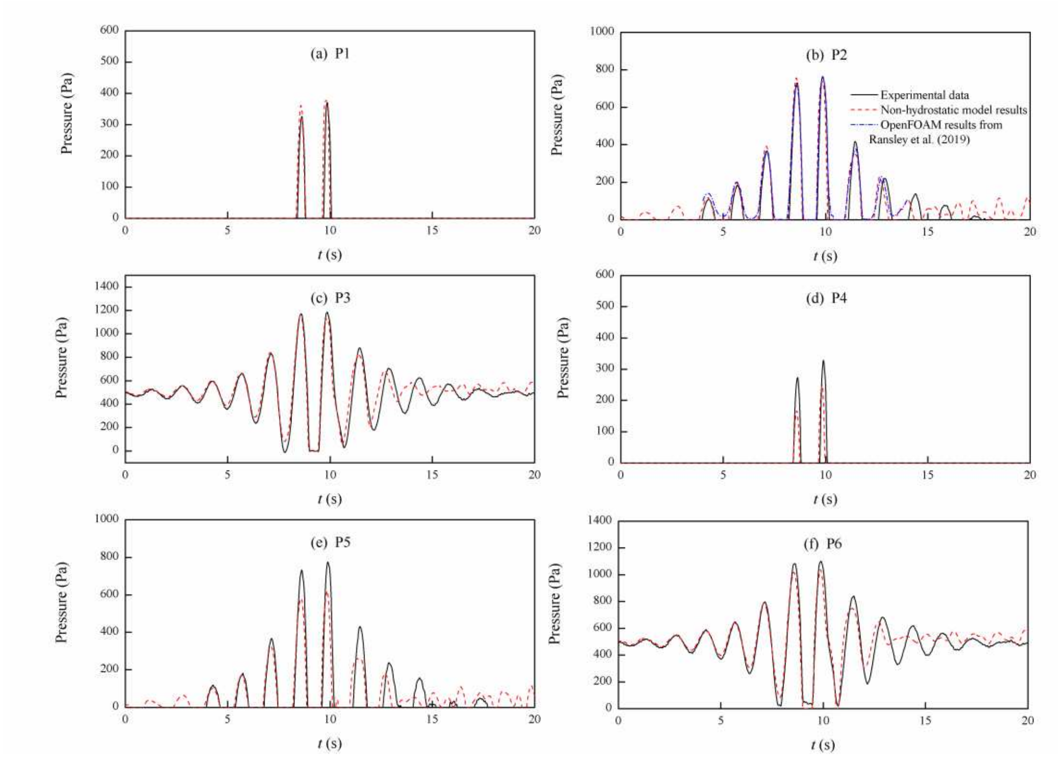

Fig. 14 Comparisons of the time histories of the pressure between the present model results and experimental data for Case 12BT1.

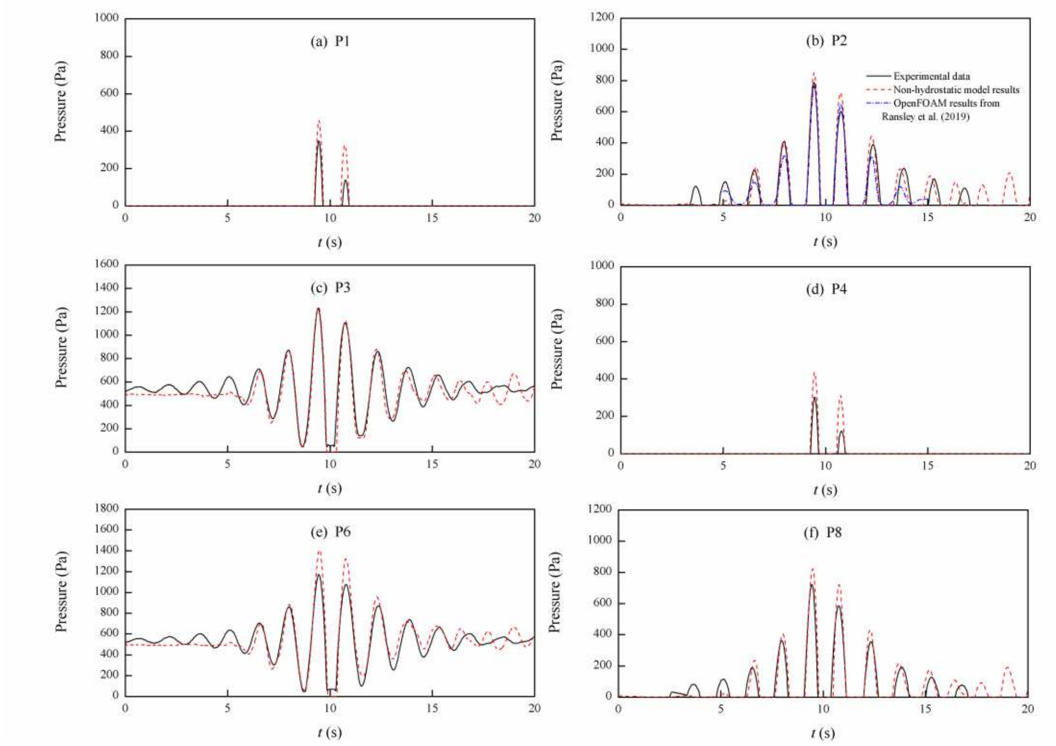

Fig. 15 Comparisons of the time histories of the pressure between the present model results and experimental data for Case 22BT1.

The computational efficiency for the two sets of non-hydrostatic models is presented in Table 4. Both non-hydrostatic models were run on the same computational environment as that mentioned in the previous example and were also implemented in parallel. For Case 12BT1, the published CPU time (Yan et al., 2019) spent by the qaleFOAM is also provided for reference. The qaleFOAM (Wang et al., 2018) is a hybrid numerical model, in which the computational domain is divided into the fully nonlinear potential theory (FNPT) domain and NSE domain. The FNPT domain is computed by the quasi-arbitrary Lagrangian Eulerian finite element method (QALE-FEM) model (Ma and Yan, 2009), while the solution in the NSE domain around the structure is obtained by the OpenFOAM solver. The total CPU times for the non-hydrostatic model with the implementation of Eq. (10) are 23.60 h and 23.32 h for Case 12BT1 and Case 22BT1, respectively, while the computational time for the non-hydrostatic model with the implementation of the NBCP are 30.90 h and 29.12 h for Case 12BT1 and Case 22BT1, respectively. The non-hydrostatic model with the implementation of Eq. (10) is also computationally more efficient than the non-hydrostatic model with the implementation of the NBCP.

The CPU time required by the qaleFOAM is 35.96 h for Case 12BT1. One may notice that the computational environment, simulation time and the total grid number are different between the two non-hydrostatic models and the qaleFOAM. The present simulations are conducted on quad-core CPUs with a base frequency of 4.2 GHz and 8 MB L3 cache, while qaleFOAM is run on a workstation with 8-core CPUs, which have a base frequency of 2.6 GHz and 20 MB L3 cache. The simulation time for qaleFOAM is longer than those for the two non-hydrostatic models, but two non-hydrostatic models employs more grid numbers than qaleFOAM. However, it can be inferred that the non-hydrostatic model with the implementation of Eq. (10) is comparable to qaleFOAM in terms of efficiency.

Table 4 Computational efficiency for focused wave interactions with a fixed FPSO

Model	Case ID	Computational environment	Simulation time (s)	Total grid number	CPU time (h)
Non-hydrostatic model with Eq. (10)	Case 12BT1	CPU: Intel(R) Core(TM) i7-7700K, 4 cores, 4.2 GHz; L3: 8 MB	20	3,024,000	23.60
	Case 22BT1				23.32
Non-hydrostatic model with the NBCP	Case 12BT1	CPU: Intel(R) Core(TM) i7-7700K, 4 cores, 4.2 GHz; L3: 8 MB	20	3,024,000	30.90
	Case 22BT1				29.12
qaleFOAM	Case 12BT1	CPU: Xeon E5-2660, 8 cores, 2.6 GHz L3: 20 MB	30	1,960,000	35.96

5. Conclusions

In this paper, an efficient 3D non-hydrostatic model, based on two former models, is developed to simulate the interaction between nonlinear waves and fixed floating structures. The model utilizes a semi-implicit, fractional step algorithm to solve the incompressible Euler equation and treats the free surface as a single-valued function of horizontal positions. The combination of the immersed boundary method and the global continuity equation in the pressurized region is proposed in the model, which renders an efficient solution of the Poisson equation.

The accuracy and efficiency of the developed model is evaluated by two examples. The overall good agreement between the present model results and experimental data indicate that the developed model is capable of accurately predicting the interaction between nonlinear waves and fixed floating structures. The present model with the implementation of Eq. (10) is more efficient than OpenFOAM for the first example of regular wave interactions with a box-shaped ship and is comparable to qaleFOAM in terms of efficiency for the second example of focused wave interactions with a fixed FPSO. In general, the developed 3D non-hydrostatic model can be viewed as an alternative for the prediction of nonlinear wave interactions with fixed floating structures.

CRediT authorship contribution statement

Congfang Ai: Conceptualization, Methodology, Software, Validation, Writing - Original Draft, Funding acquisition. **Yuxiang Ma**: Conceptualization, Methodology, Funding acquisition. **Changfu Yuan**: Methodology, Validation. **Zhihua Xie**: Conceptualization, Writing - Review & Editing. **Guohai Dong**: Supervision, Funding acquisition. **Thorsten Stoesser**: Supervision, Writing - Review & Editing.

Acknowledgments

This research is financially supported by the National Natural Science Foundation of China (Grant No. 52171248, 51720105010, 51979029), LiaoNing Revitalization Talents Program (Grant No. XLYC1807010) and the Fundamental Research Funds for the Central Universities (Grant No. DUT2019TB02, DUT21LK01).

References

Ai, C., Ding, W., 2016. A 3D unstructured non-hydrostatic ocean model for internal waves. Ocean Dyn. 66, 1253-1270.

Ai, C., Ding, W., Jin, S., 2014. A general boundary-fitted 3D non-hydrostatic model for nonlinear focusing wave groups. Ocean Eng. 89, 134-145.

Ai, C., Jin, S., 2012. A multi-layer non-hydrostatic model for wave breaking and run-up. Coast. Eng. 62, 1-8.

Ai, C., Jin, S., Lv, B., 2011. A new fully non-hydrostatic 3D free surface flow model for water wave motions. Int. J. Numer. Methods Fluids 66, 1354-1370.

Ai, C., Ma, Y., Yuan, C., Dong, G., 2019a. Development and assessment of semi-implicit nonhydrostatic models for surface water waves. Ocean Model. 144, 101489.

Ai, C., Ma, Y., Yuan, C., Dong, G., 2018. Semi-implicit non-hydrostatic model for 2D nonlinear wave interaction with a floating/suspended structure. Eur. J. Mech. B-Fluids

72, 545-560.

Ai, C., Ma, Y., Yuan, C., Dong, G., 2019b. A 3D non-hydrostatic model for wave interactions with structures using immersed boundary method. Comput. Fluids 186, 24-37.

Bihs, H., Chella, M.A., Kamath, A., Arntsen, Ø., 2017. Numerical investigation of focused waves and their interaction with a vertical cylinder using REEF3D. J. Offshore Mech. Arct. Eng. 139, 041101.

Bihs, H., Kamath, A., Aggarwal, A., Pakozdi, C., 2019. Efficient Wave Modeling Using Nonhydrostatic Pressure Distribution and Free Surface Tracking on Fixed Grids. J. Offshore Mech. Arct. Eng. 141, 041805.

Casulli, V., Stelling, G.S., 1998. Numerical simulation of 3D quasi-hydrostatic, free surface flows. J. Hydraul. Eng.-ASCE 124, 678-686.

Casulli, V., Stelling, G.S., 2013. A semi-implicit numerical model for urban drainage systems. Int. J. Numer. Methods Fluids 73, 600-614.

Fadlun, E.A., Verzicco, R., Orlandi, P., Mohd-Yusof, J., 2000. Combined immersed-boundary finite-difference methods for three-dimensional complex flow simulations. J. Comput. Phys. 161, 35-60.

Hu, Z.Z., Greaves, D., Raby, A., 2016. Numerical wave tank study of extreme waves and wave-structure interaction using OpenFoam®. Ocean Eng. 126, 329-342.

Lai, Z., Chen, C., Cowles, G.W., Beardsley, R.C., 2010. A nonhydrostatic version of FVCOM: 1. Validation experiments. J. Geophys. Res. 115, C11010.

Li, Q, Wang, J.H., Yan, S., Gong, J.Y., Ma, Q.W., 2018. A zonal hybrid approach coupling FNPT with OpenFOAM for modelling wave-structure interactions with action of current. Ocean Syst. Eng. 8, 381-407.

Ma, G., Shi, F., Kirby, J.T., 2012. Shock-capturing non-hydrostatic model for fully dispersive surface wave processes. Ocean Model. 43-44, 22-35.

Ma, G., Farahani, A.A., Kirby, J.T., Shi, F., 2016. Modeling wave-structure interactions by an immersed boundary method in a σ-coordinate model. Ocean Eng. 125, 238-247.

Ma, Q.W., Yan, S., 2009. QALE-FEM for numerical modelling of non-linear interaction between 3D moored floating bodies and steep waves. Int. J. Numer. Methods Eng. 78, 713-756.

Ma, Y., Yuan, C., Ai, C., Dong, G., 2019. Comparison between a non-hydrostatic model and OpenFOAM for 2D wave-structure interactions. Ocean Eng. 183, 419-425.

Mohseni, M., Esperanca, P.T., Sphaier, S.H., 2018. Numerical study of wave run-up a fixed and vertical surface-piercing cylinder subjected to regular, non-breaking waves using OpenFOAM. Appl. Ocean Res. 79, 228-252.

Oishi, Y., Piggott, M.D., Maeda, T., Kramer, S.C., Collins, G.S., Tsushima, H., Furumura, T., 2013. Three-dimensional tsunami propagation simulations using an unstructured mesh finite element model. J. Geophys. Res.-Solid Earth 118, 2998-3018.

Ransley, E., Yan, S., Brown, S.A. et al, 2019. A blind comparative study of focused wave interactions with a fixed FPSO-like structure (CCP-WSI Blind Test Series 1). Int. J. Offshore Polar Eng. 29, 113-127.

Rijnsdorp, D.P., Zijlema, M., 2016. Simulating waves and their interactions with a restrained ship using a non-hydrostatic wave-flow model. Coast. Eng. 114, 119-136.

Rijnsdorp, D.P., Hansen, J.E., Lowe, R.J., 2018. Simulating the wave-induced response of a submerged wave-energy converter using a non-hydrostatic wave-flow model. Coast. Eng. 140, 189-204.

Stansby, P.K., Zhou, J.G., 1998. Shallow-water flow solver with non-hydrostatic pressure: 2D vertical plane problems. Int. J. Numer. Methods Fluids 28, 514-563.

Vukčević, V., Jasak, H., Malenica, S., 2016. Decomposition Model for Naval Hydrodynamic Applications, Part I: Computational Method. Ocean Eng. 121, 37-46.

Wang, J., Ma, Q.W., Yan, S., 2018. A fully nonlinear numerical method for modeling wave-structure interactions. J. Comput. Phys. 369, 173-190.

Wang, D.G., Zou, Z.L., Tham, L.G., 2011. A 3-D time-domain coupled model for non-linear waves acting on a box-shaped ship fixed in a harbor. China Ocean Eng. 25, 441-456.

Xie, Z., Lu, L., Stoesser, T., Lin, J., 2017. Numerical simulation of three-dimensional breaking waves and its interaction with a vertical circular cylinder. J. Hydrodyn. 29, 800-804.

Xie, Z., Stoesser, T., 2020. Two-phase flow simulation of breaking solitary waves over surface-piercing and submerged conical structures. Ocean Eng. 213, 107679.

Xie, Z., Stoesser, T., Yan, S., Ma, Q., Lin, P., 2020. A Cartesian cut-cell based multiphase flow model for large-eddy simulation of three-dimensional wave-structure interaction. Comput. Fluids 213, 104747.

Yan, S., Li, Q., Wang, J., Ma, Q., Xie, Z., Stoesser, T., 2019. Comparative numerical study on focusing wave interaction with FPSO-like structure. Int. J. Offshore Polar Eng. 29, 149-157.

Zhan, J., Chen, X., Gong, Y., Hu, W., 2017. Numerical investigation of the interaction between an inverse T-type fixed/floating breakwater and regular/irregular waves. Ocean Eng. 137, 110-119.

Zijlema, M., Stelling, G.S., Smit, P., 2011. SWASH: an operational public domain code for simulating wave fields and rapidly varied flows in coastal waters. Coast. Eng. 58, 992-1012.